Materials Today Communications 52 (2026) 114992

Contents lists available at ScienceDirect

Materials Today Communications

journal homepage: www.elsevier.com/locate/mtcomm

A hybrid CFD–Machine Learning framework for efficient permeability prediction in 3D-printed bone scaffold design

Maedeh Amirpour [a,b,*], Eric Feng [a], Ali Entezari [c]

[a] Department of Engineering Science and Biomedical Engineering, University of Auckland, New Zealand
[b] Centre for Advanced Materials, Manufacturing and Design, University of Auckland, New Zealand
[c] School of Biomedical Engineering, Faculty of Engineering and Information Technology, University of Technology Sydney, Sydney, NSW 2007, Australia

ARTICLE INFO

Keywords:
Bone scaffold design
3D printing
Permeability prediction
Computational fluid dynamics
Machine learning
Genetic algorithm

ABSTRACT

The design of bone scaffolds with controlled permeability is critical for successful osseointegration and nutrient transport in tissue engineering applications. This study presents a fully automated hybrid framework that combines computational fluid dynamics (CFD) and machine learning (ML) for accurate permeability prediction, supporting patient-specific design of 3D printed bone scaffolds. The proposed end-to-end, scalable, high-throughput framework enables systematic data generation and ML-based surrogate modelling of permeability across complex scaffold architectures. Extracted geometric and flow-related features form the basis for ML modelling using algorithms such as Decision Trees, Random Forest, Gradient Boosting, as well as more advanced models, such as artificial neural networks (ANN), specifically Multilayer Perceptron (MLP) architectures. The results demonstrate that an MLP-based surrogate model achieves high predictive accuracy ($R^2 \sim 0.9989$) and robustness across diverse scaffold designs. The scaffold topologies considered include triply periodic minimal surface (TPMS) structures such as Primitive, Gyroid and Diamond, as well as graph-based lattice structures including Simple Cubic, Body Centered Cubic (BCC) and Truncated Octahedron. Beyond permeability prediction, the framework enables time-efficient design exploration and provides a pathway towards patient-specific optimisation of scaffolds with tailored fluid transport and mechanical properties. Overall, the integration of automated design and simulation with ML offers a scalable solution for next-generation regenerative medicine and additive manufacturing.

1. Introduction

Bone tissue engineering (BTE) scaffolds are porous 3D structures designed to facilitate the regeneration of large or non-healing bone defects that exceed the body's natural healing capacity [1]. Critical-sized bone defects remain a persistent clinical challenge because conventional treatments—autografts, allografts, and dense, off-the-shelf implants—struggle to simultaneously match anatomical shape, mechanical behaviour, and the biological demands of the regenerating tissue [2]. An ideal bone scaffold must satisfy multiple, often competing, requirements, including sufficient mechanical strength, biocompatibility, interconnected porosity, and favourable mass transport characteristics to enable cell migration, vascularisation, and nutrient exchange [3–6]. Within this design space, permeability—the effective ease with which a fluid percolates through the porous architecture—is a first-order design parameter because it governs nutrient and oxygen delivery, removal of metabolic waste, and the magnitude/distribution of fluid--flow–induced wall shear stress (WSS) experienced by cells [7,8]. Bone tissue engineering studies consistently show that permeability (together with pore size, interconnectivity, tortuosity, and specific surface area) modulates cell migration, angiogenesis, and differentiation, and that "good" permeability targets are architecture- and tissue-context–dependent rather than universal [9–11].

Because permeability in porous scaffolds emerges directly from the underlying pore architecture such as pore size and tortuosity, it cannot be tuned independently of geometry. Achieving target permeability ranges requires precise architectural control at the unit-cell and meso-scale levels. This structural dependence naturally shifts the design problem from material selection alone toward geometry-driven optimisation. Therefore, manufacturing technologies capable of fabricating highly controlled and reproducible porous architectures are essential for translating permeability targets into functional scaffold designs.

* Corresponding author at: Department of Engineering Science and Biomedical Engineering, University of Auckland, New Zealand.
E-mail address: m.amirpourmolla@auckland.ac.nz (M. Amirpour).

https://doi.org/10.1016/j.mtcomm.2026.114992
Received 10 February 2026; Received in revised form 4 March 2026; Accepted 12 March 2026
Available online 13 March 2026
2352-4928/© 2026 The Author(s). Published by Elsevier Ltd. This is an open access article under the CC BY license (http://creativecommons.org/licenses/by/4.0/).

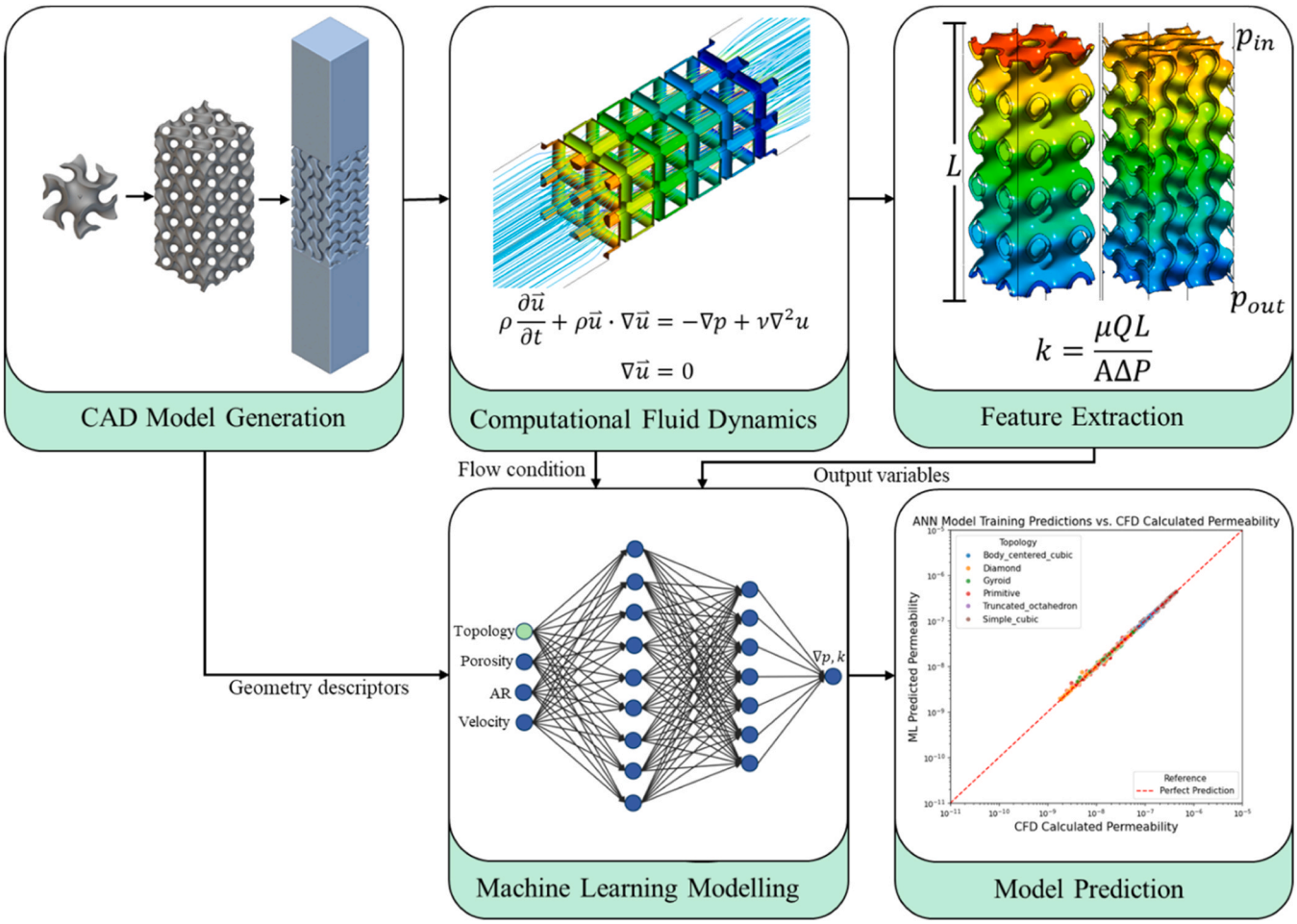


Fig. 1. Semi-automatic workflow pipeline.

Recent advances in additive manufacturing (AM) have enabled unprecedented control over scaffold architecture, allowing the fabrication of complex, highly ordered porous structures with tunable geometrical features [12–16]. In particular, lattice-based scaffolds and triply periodic minimal surface (TPMS) architectures have attracted significant attention due to their high surface-to-volume ratios, smooth curvature, and favourable mechanical and transport properties [17,18]. Comparative computational and experimental studies indicate that, at matched porosity, topology can shift permeability by orders of magnitude. For instance, gyroid sheets can exhibit higher permeability than certain diamond designs at the same nominal porosity [19,20], while other reports find diamond or octet configurations outperforming TPMS in specific flow regimes—differences that reflect pore-scale tortuosity, throat size, and the presence of recirculation zones [21]. Moreover, pressure drop is sensitive to Reynolds number [22], and non-Newtonian blood rheology [23], further complicating "rules of thumb". These findings underscore why permeability cannot be inferred from porosity alone and must be quantified for the intended geometry and physiological flow conditions. When combined with medical imaging techniques such as computed tomography (CT), AM enables the creation of patient-specific scaffolds that can be tailored to individual anatomical and physiological requirements [24]. However, this increased design freedom has also introduced new challenges in predicting scaffold performance, especially with respect to fluid transport behaviour.

While empirical permeability relationships, such as Kozeny–Carman-type models, provide qualitative insight into permeability–porosity trends, they are often insufficient for complex scaffold architectures where pore morphology, tortuosity, aspect ratio, and flow regime interact nonlinearly for higher Reynolds number [25,26]. As a result, computational fluid dynamics (CFD) has become the dominant tool for quantitatively evaluating permeability in additively manufactured scaffolds [27,28]. Pore scale CFD is accurate and versatile (it can incorporate Newtonian/non Newtonian fluids, device specific boundary conditions, and realistic printing artifacts), but it is time and resource intensive [6,29]. Each new geometry requires meshing intricate channels, model set up, solver tuning, and post processing to extract pressure gradients to calculate permeability—steps that do not scale well when exploring large parametric spaces (for example: topology × porosity × aspect ratio × flow). Meanwhile, Kozeny–Carman models provide fast estimates but must be refitted to architecture specific constants (tortuosity and specific surface area surrogates), and they struggle with complex, graded, or mixed topology scaffolds typical of patient specific designs [30–32].

To mitigate CFD cost, several groups have (i) standardized CFD pipelines for common TPMS units and parameter sweeps [33,34]; (ii) combined CFD with experiments to cross-validate permeability across porosity and pore sizes [35]; and (iii) proposed data-driven surrogates that regress permeability (and sometimes WSS) on geometric descriptors [36]. For example, numerical–experimental comparisons on gyroid/diamond/Schwarz TPMS at fixed porosity demonstrated strong topology effects on Darcy permeability [36]; other studies reported how Reynolds number and non-Newtonian viscosity alter both permeability and WSS predictions—even reversing trends obtained under Newtonian assumptions [37]. Also, empirical or hybrid models have extended Kozeny–Carman with topology-dependent constants or have proposed direct correlations between geometry, permeability, and WSS to bypass

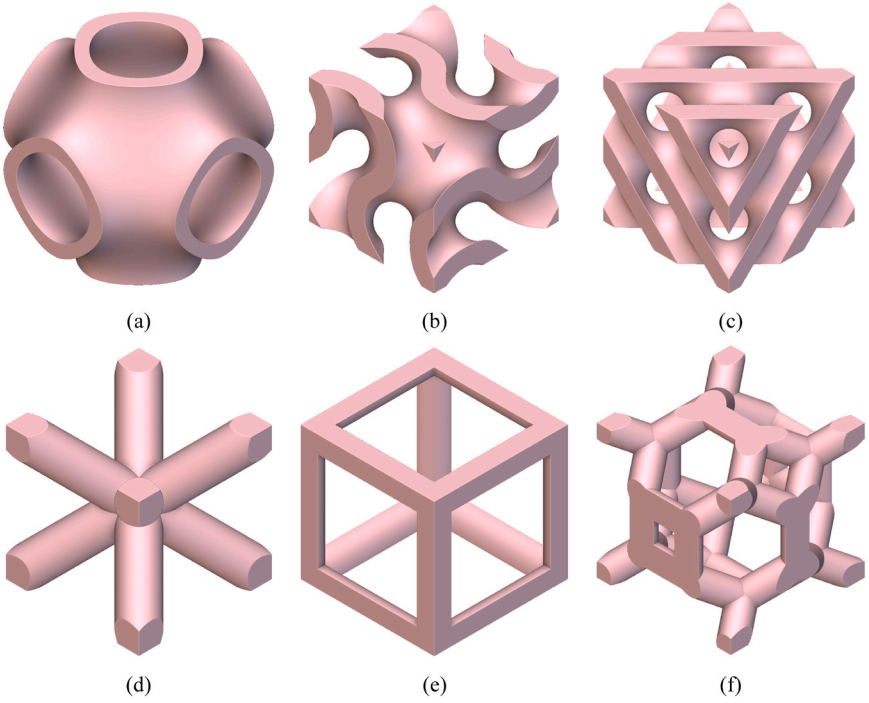


Fig. 2. Topology unit cell types - (a) Primitive, (b) Gyroid, (c) Diamond, (d) Body Centered Cubic (BCC), (e) Simple Cubic (f), and Truncated Octahedron (TO).

full CFD [38–40]. Despite progress, most workflows remain semi-manual and tuned to limited geometry families, which constrains their use for rapid, patient-specific design iterations.

In a subject-specific context, surgeons and engineers need to explore dozens–hundreds of candidate scaffold variants (varying topology, porosity, strut thickness/aspect ratio, and local grading) under physiologically plausible flows to strike the best compromise between mechanical stability and mass transport [41,42]. Pure CFD becomes a bottleneck: running hundreds to thousands of pore-scale simulations can consume days to weeks, delaying decision-making and limiting the breadth of the design space explored pre-operatively. Also, the intrinsic heterogeneity and structural disorder of porous scaffolds make it difficult to establish an explicit analytical relationship between permeability and pore morphology. The permeability–structure interaction is inherently nonlinear and strongly dependent on multiscale geometric features, rendering conventional closed-form modelling approaches inadequate for complex architectures. Equally, relying on generic, closed-form permeability formulas can mislead when applied to complex TPMS–lattice mixtures that deviate from their calibration domain. Thus, there is a need for a scalable, automated, and generalizable prediction pipeline that preserves CFD-level fidelity yet delivers near-real-time estimates once trained. In recent years, however, advances in big data analytics and artificial intelligence have enabled accurate predictive capabilities without reliance on extensive experimental campaigns or computationally intensive modelling workflows. Machine learning (ML), a major branch of artificial intelligence, has undergone rapid development over the past two decades. ML encompasses a family of data-driven algorithms designed to infer complex functional relationships from training data, identifying optimal predictive models that maximise generalisation performance. Rather than prescribing explicit physical equations, ML algorithms learn patterns directly from data, making them particularly suitable for capturing high-dimensional, nonlinear interactions between microstructural descriptors and transport properties such as permeability [43]. The adoption of ML across diverse scientific and engineering domains has expanded rapidly in recent years. In Biomechanical, physics–ML pipelines accelerate implant and scaffold design by training surrogates on FEM/CFD or remodeling simulations and embedding them in active-learning, Bayesian, or genetic optimization loops [44]. The key remaining gaps for permeability-focused scaffold design are generalization beyond idealized architecture families and robust prediction/validation of localized transport extremes using experimentally grounded CFD–ML datasets [45]. In this paper a hybrid method that combine CFD and ML was applied to predict permeability.

We use high-fidelity CFD to generate a large, diverse dataset spanning relevant scaffold architectures and flow regimes; extract physically informed geometric/flow features; and train supervised ML models to learn the permeability mapping. Notably, in porous media research, hybrid models that pair Artificial Neural Networks (ANNs) with evolutionary search (e.g., GA-optimized an architectures) have already achieved near-perfect prediction accuracy on CFD-derived datasets, while revealing which microstructural variables (such as porosity and tortuosity) most strongly govern permeability.

We introduce a fully automated hybrid framework for permeability prediction of 3D-printed bone scaffolds that (i) programmatically generates large libraries of scaffold CADs across both TPMS and strut-based lattices (with tuneable porosity and aspect ratio), (ii) executes batch CFD under physiologically motivated laminar flow conditions to compute apparent Darcy permeability, and (iii) learns fast, accurate surrogates using bayesian optimisation on a feature set comprising topology, porosity, aspect ratio, and inlet velocity.

Our CFD–ML framework learns these coupled effects directly from data, rather than assuming a single parametric law. It therefore supports topology aware tuning and offers interpretable sensitivity analyses to guide designers toward architectures that meet both transport and mechanical constraints.

2. Methodology

A semi-automatic workflow pipeline as shown in Fig. 1 was developed to enable the large amounts of synthetic fluidic permeability data to be generated. First, the generation of fluid domains corresponding to each scaffold design across a full parameter sweep was fully automated through the integration of nTopology (nTop) and Python. Subsequently, computational fluid dynamics (CFD) simulations were executed for each design in ANSYS Fluent using Python-based scripting (explained at §2.2)

Table 1
Design Parameters Table.

Design Parameters	Range
Topology	TPMS-Gyroid TPMS-Diamond TPMS-Primitive Body Centered Cubic (BCC) Truncated Octahedron Simple Cubic
Porosity (%)	50 – 80 (70 – 85 for TO)
Aspect Ratio	1:0.5 1:1 1:1.5
Velocity ($mm \cdot s^{-1}$)	0.1 1 10

to estimate the scaffold's apparent permeability under physiologically relevant flow conditions.

All computations in this study were performed on a laboratory computer equipped with a 13th Gen Intel i7–13700 CPU and an Nvidia T400 GPU with 4 GB VRAM.

2.1. Data generation automation process

The CFD data generation process was semi-automated using nTop Automate (previously called nTopCL), which executes nTop files through a command-line interface, enabling a systematic generation and storage of geometries as STL files. Porous scaffold architectures were parameterised within nTop and accessed via the command-line interface, where input parameters and outputs were defined using structured JSON files. Python was employed to programmatically generate, manage, and execute all JSON configurations, thereby automating the geometry creation process across the full design space.

The generated STL files were subsequently imported into ANSYS Fluent, where Python-based scripting was used to automate geometry preprocessing, naming conventions, meshing, solver setup, and permeability calculations. Inlet velocity was parameterised using ANSYS Design Points, allowing multiple flow conditions to be evaluated for each scaffold topology. Simulation outputs for each configuration were automatically exported as CSV files, facilitating efficient data aggregation and downstream preparation for machine-learning model development.

2.2. CAD model generation

The computational fluid domain consisted of a rectangular channel with overall dimensions of $75 \times 10 \times 10$ mm, partitioned into three sections corresponding to the inlet (upstream), the porous scaffold region and the outlet (downstream). The unit cell size of each scaffold was 5 mm, resulting in two unit cells across the width of the domain. The porous scaffold region extended 25 mm in the streamwise direction, corresponding to five unit cells in length. The selected scaffold length and width were informed by prior convergence studies. Specifically, Asbai-Ghoudan et al. [46] showed that a minimum of four unit cells in the flow direction is sufficient to achieve convergence of the pressure gradient, while two unit cells in the transverse direction effectively eliminate boundary effects when symmetry boundary conditions are applied to the lateral faces of the fluid domain (shown in Fig. 3). A velocity inlet was applied at the upstream face, paired with a pressure outlet downstream face. This geometry is entirely generated through nTop, which is then imported into Ansys Spaceclaim as an STL file, where shrink-wrapping was applied to ensure a nonproblematic watertight, CFD-ready fluid volume. Boundary condition named selections (velocity_inlet, pressure_outlet, symmetry_walls) were created programmatically in SpaceClaim using scripting to support automated simulation setup.

The variations in scaffold architecture explored were both graph-based lattice structures and TPMS unit cell topologies. In addition to lattice topology, porosity and aspect ratio were systematically varied. The influence of Reynolds number on fluidic permeability was also examined by varying inlet flow conditions, enabling assessment of permeability behaviour across different flow regimes. A topology representation of the constitutive unit cell of the scaffolds is shown in Fig. 2.

The TPMS unit cell topologies explored Schwarz Primitive, Gyroid and Diamond, whereas the graph unit cell topologies explored are Body Centered Cubic (BCC), Simple Cubic (SC) and Truncated Octahedron (TO). These topologies were chosen for their prevalence in BTE applications, as demonstrated by [46–48]. The porosity ranges were between 50% and 80%, and the aspect ratios were 1:0.5, 1:1 and 1:1.5. However, for TO, the porosities were found to be unphysical below 70% for a 1:0.5 aspect ratio and 80% for 1:1 and 1:1.5 aspect ratios. The summary of the variations in geometry descriptors considered can be found in Table 1.

2.3. Computational fluid dynamic (CFD)

Ansys Workbench scripting was employed to automate the entire process CFD workflow, encompassing geometry import, meshing, solver setup, simulation execution, and export of permeability results as CSV files. To enable robust automation, all STL geometries were standardised to ensure compatibility with a unified scripting framework.

Meshing was performed using Fluent Meshing as it is GPU-enabled, allowing faster computation compared to Ansys Mechanical. The Watertight Geometry workflow was used to generate polyhedral volume cells to efficiently resolve the complex internal flow paths of the porous scaffold region. Six inflation layers were applied at solid-fluid interfaces to capture the laminar boundary layer effects near scaffold surfaces. Due to limitations in fully automating local mesh sizing for highly complex scaffold geometries, no explicit local sizing was applied within Fluent. Instead, the STL geometry exported from nTop was first processed using the shrink-wrapping tool in ANSYS SpaceClaim to generate a watertight surface and remove overlapping faces. During this preprocessing step, a large maximum edge length (100 mm) was specified only to minimise unnecessary surface refinement and reduce the number of faces generated during shrinkwrapping. The effective CFD mesh resolution was governed by a minimum edge length of 0.1 mm, which enabled adequate capture of the complex internal curvature of the porous scaffold while maintaining a coarser mesh in the upstream and downstream

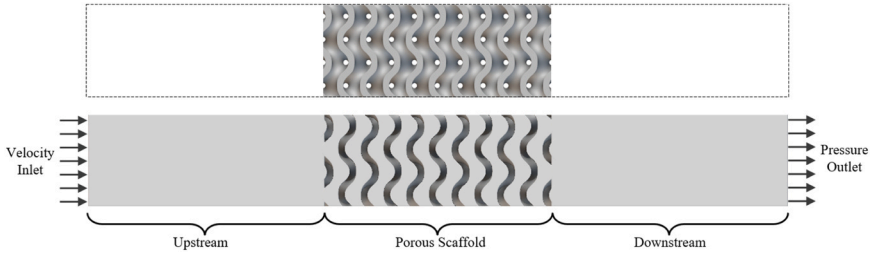


Fig. 3. Fluid domain setup.

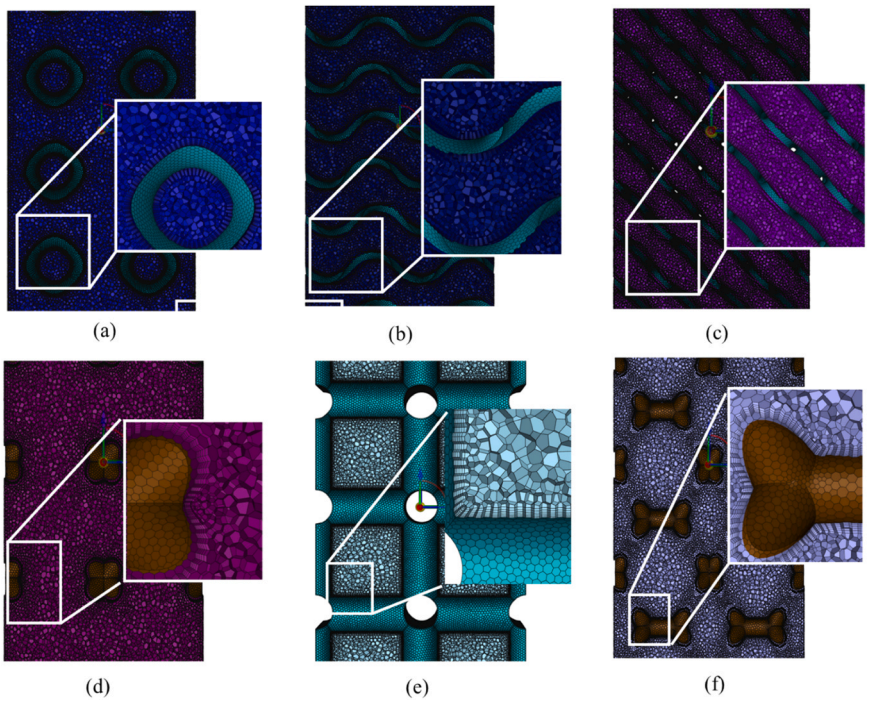


Fig. 4. Mesh generation for (a) Primitive, (b) Gyroid, (c) Diamond, (d) Body Centered Cubic (BCC) (e) Simple Cubic (f) Truncated Octahedron topologies.

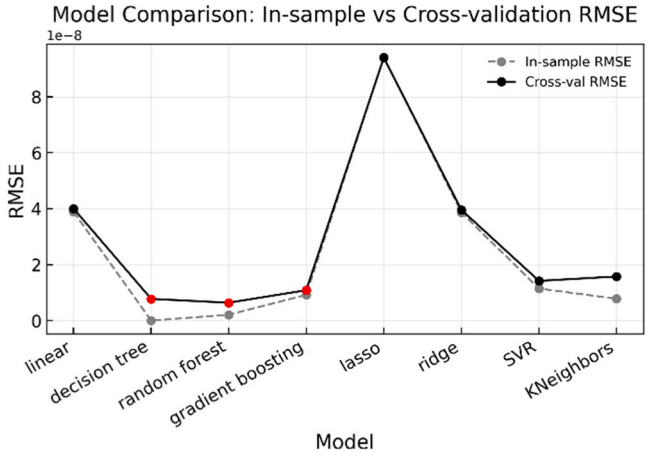


Fig. 5. Performance comparison with classical ML algorithms.

Table 3
Decision Tree hyperparameter search space.

Hyperparameter	Range/Configuration
regressor_reg_criterion	'squared_error', 'friedman_mse'
regressor_reg_min_samples_split	2 – 100
regressor_reg_min_samples_leaf	1 – 10
regressor_reg_max_features	1.0, 'sqrt', 'log2'
regressor_reg_max_depth	3 – 30

Table 4
Random Forest hyperparameter search space.

Hyperparameter	Range/Configuration
regressor_reg_n_estimators	50 – 800
regressor_reg_min_samples_split	2 – 100
regressor_reg_min_samples_leaf	1 – 4
regressor_reg_max_features	1.0, 'sqrt', 'log2'
regressor_reg_max_depth	None – 40

Table 2
Gradient Boosting hyperparameter search space.

Hyperparameter	Range/Configuration
regressor_reg_subsample	0.6 – 1.0
regressor_reg_n_estimators	100 – 800
regressor_reg_min_samples_split	2 – 10
regressor_reg_min_samples_leaf	1 – 5
regressor_reg_max_features	None, 'sqrt', log2'
regressor_reg_max_depth	2 – 5
regressor_reg_learning_rate	0.01 – 0.2

Table 5
MLP hyperparameter search space.

Hyperparameter	Range/Configuration
num_epoch	800 – 1400
learning_rate	1×10^{-4} – 3.5×10^{-4}
batch_size	16 – 128
architecture	[64, 32]
	[64, 64, 32]
	[128, 64, 32]
	[128, 64, 32, 16]
	[128, 128, 64, 32]
	[256, 128, 64, 32]
activation_function	ReLU
optimiser	ADAM
c-v_evaluation_interval	20
patience	5

flow regions.

A mesh convergence study was applied to ensure the model permeability values were independent of the mesh resolution. The convergence analysis focused on the most demanding flow scenarios, namely gyroid scaffold with extreme porosity values evaluated at the highest Reynolds number considered in this study. Low-porosity configurations exhibit increased flow tortuosity and larger pressure gradients, while

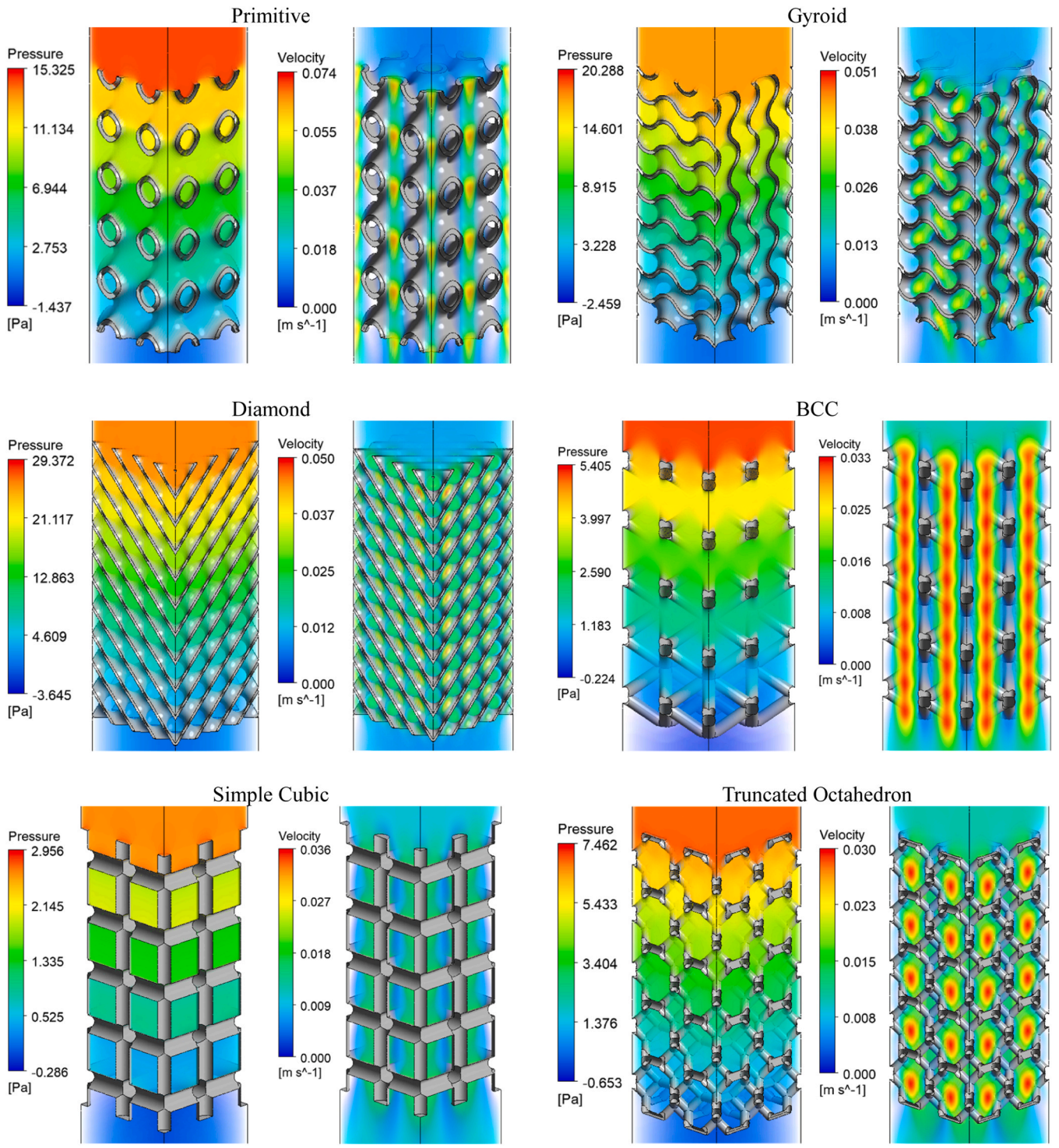


Fig. 6. Pressure and velocity distributions of fluid volume for different scaffolds at 80% porosity, 1:1 aspect ratio.

high-porosity configurations result in elevated pore-scale Reynolds numbers due to enlarged flow channels. Based on these considerations, the final mesh employed surface triangular elements ranging from 0.05 to 0.13 mm, and a maximum polyhedral cell length of 0.27 mm in the volume mesh. The configuration was found to provide mesh-independent permeability predictions while maintaining stable solver convergence across all simulated cases. The final mesh configuration after convergence testing for all six scaffold topologies is shown in Fig. 4.

Blood flow through the porous scaffold region was modelled as an incompressible Newtonian fluid with a density of 1060 kg·m^{-3} and a dynamic viscosity of 0.0035 Pa·s, consistent with reported physiological blood properties [48]. Three steady velocity inlets of 0.1, 1.0 and 10 mm·s^{-1} were prescribed to represent a range of physiological flow conditions. These values reflect spatial variations in skeletal blood perfusion as well as inter-individual differences. In particular, Salles et al. [49] shows that the time-averaged axial blood flow through the tibia cortical bone is below 1.0 mm·s^{-1} (around 0.4 mm·s^{-1} averaged among subjects), peak axial velocities can reach up to around 9.9 mm·s^{-1}. We quantify the flow regime using a pore-scale Reynolds number as follows [50]:

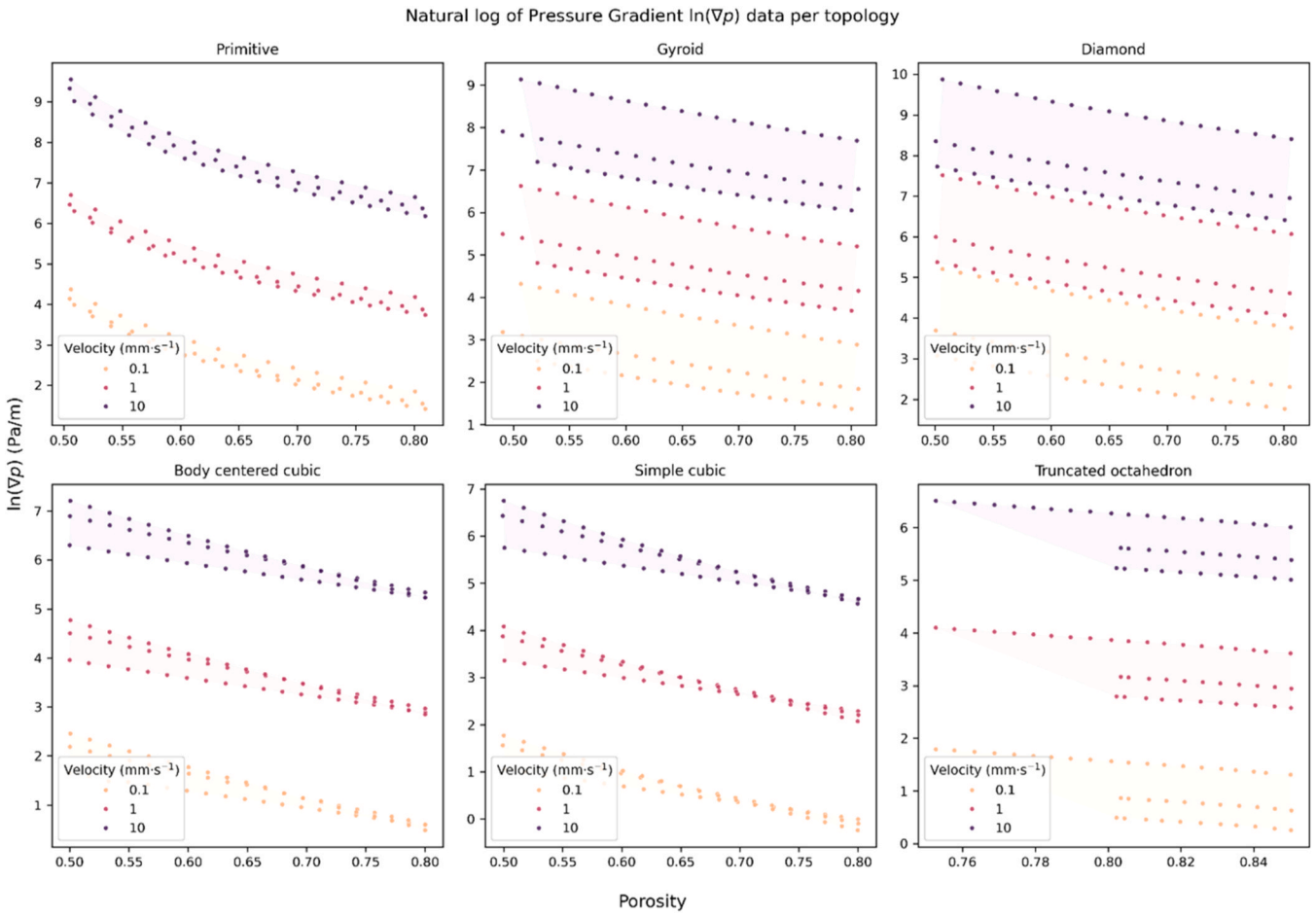


Fig. 7. Pressure gradient CFD results for all topologies with different velocity and porosity.

$$\mathrm{Re} = \frac{\rho \mathrm{U} \mathrm{D_p}}{\mu} \tag{1}$$

where U is the superficial velocity, D_p is pore size in scaffold architecture, ρ is the density, and μ is the dynamic viscosity. From Table 1, the highest pore-scale Reynolds number possible is 11.9 using a Simple Cubic scaffold at its highest fluid flow of 0.1 mm·s^{-1} and a porosity of 80%, corresponding to a strut thickness of 1.066 mm. This value is well within the steady laminar regime for pore-scale flow in additively manufactured scaffolds [51], where inertial (Forchheimer) effects may begin to appear for $\mathrm{Re_{pore}} \gtrsim 1$–10 but turbulence is not expected at the present conditions. For all simulated cases, the Reynolds number remained within the laminar flow regime; therefore, no turbulence model was applied, consistent with prior studies of flow through porous bone-like scaffolds [52]. Incompressible flow was also assumed due low Reynolds number. Hence, the steady-state Navier Stokes equation was solved using the Semi implicit method for pressure-linked equations (SIMPLE). Convergence was deemed achieved when all residuals fell below 1×10^{-4}.

Permeability calculations were done at the end of each CFD simulation using CFD-Post, following Darcy's law (Eq. 1):

$$k = \frac{\mu Q L}{A \Delta P} \tag{2}$$

where A is the cross-sectional area of the geometry and is consistent for all model runs in this case and equal to 100 mm^2. L is the length of the porous scaffold region, which again is consistent for all model runs. The pressure drop (ΔP, Pa) was calculated as the difference between the area-averaged static pressures evaluated on planar sections located at the inlet and outlet of the porous region, rather than at the external domain boundaries. The volumetric flow rate (Q, m^3·s^{-1}) through the porous region was evaluated at the domain inlet. Owing to the assumptions of steady-state and incompressible flow, the volumetric flow rate was conserved along the flow direction, making this a valid representation of the flow through the porous scaffold region. For increased fluid flow, inertial effects were observed, which was described by the Forchheimer model (Eq. 2) which includes an inertial term, or the Forchheimer coefficient β, to capture non-linearity, allowing applicability for higher Reynolds number, typically greater than 1.

$$\frac{\Delta P}{L} = \frac{\mu}{k} v + \beta \rho v^2 \tag{3}$$

Validation of the CFD model was performed by benchmarking the simulation setup against representative scenarios reported in the literature.

In particular, the study by Cracknell et al. [53] was used as a reference for the first benchmark case, in which scaffold permeability was evaluated both experimentally and numerically for a geometrically comparable porous structure using oil as the working fluid, with a density of 880 kg·m^{-3} , a dynamic viscosity of 0.2262 Pa·s. Despite differences in fluid properties, the comparison enabled assessment of the numerical formulation, boundary condition implementation, and permeability extraction methodology employed in the present study. The second benchmark case was compared with Gupta et al. [54] who investigated varying unit cell sizes (or length ratios) of a gyroid scaffold. Blood was used as the fluid, however with slightly different properties, which has a density of 1050 kg/m^3 and a dynamic viscosity of 0.004 Pa·s.

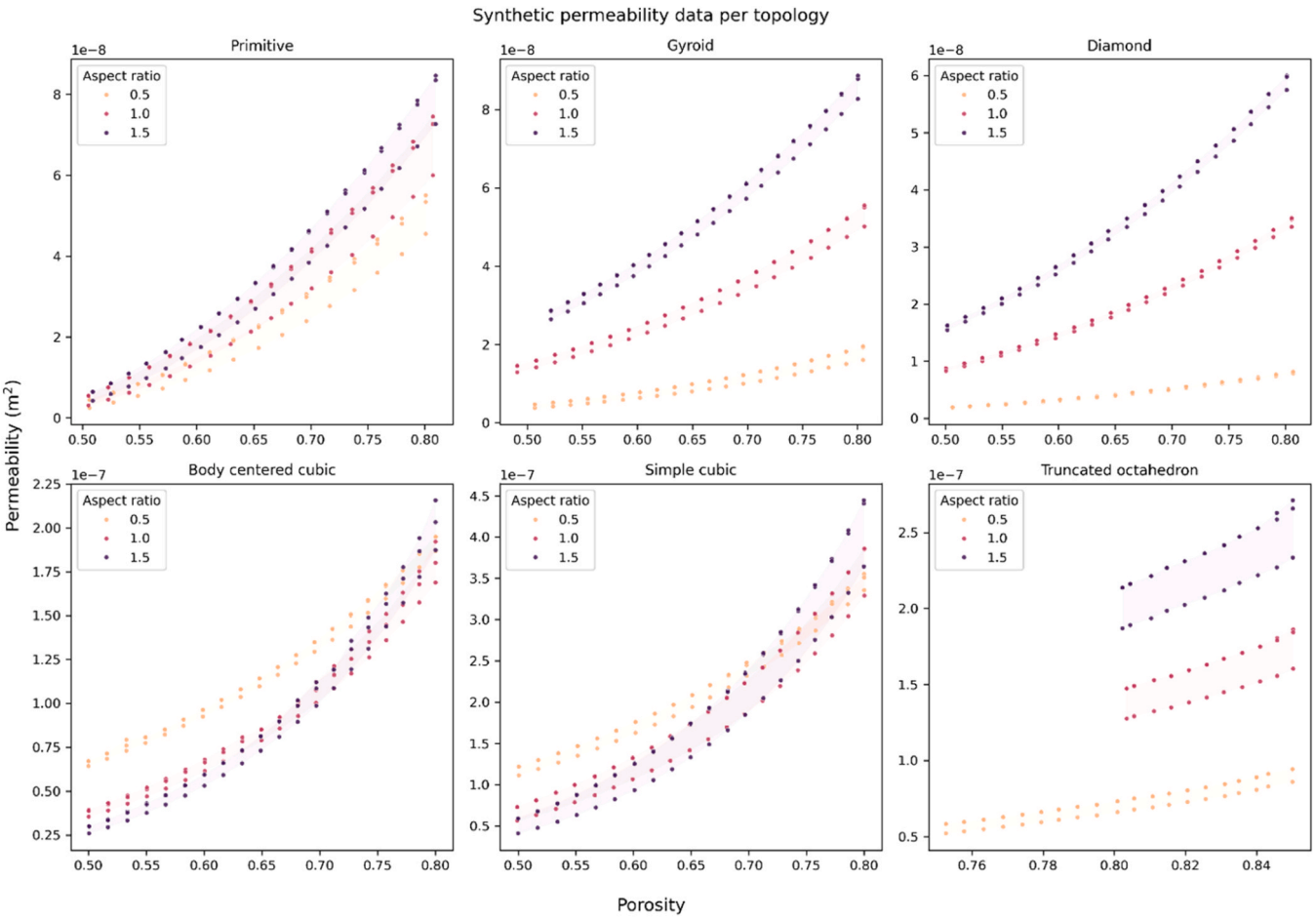


Fig. 8. Darcy's law permeability for all scaffolds.

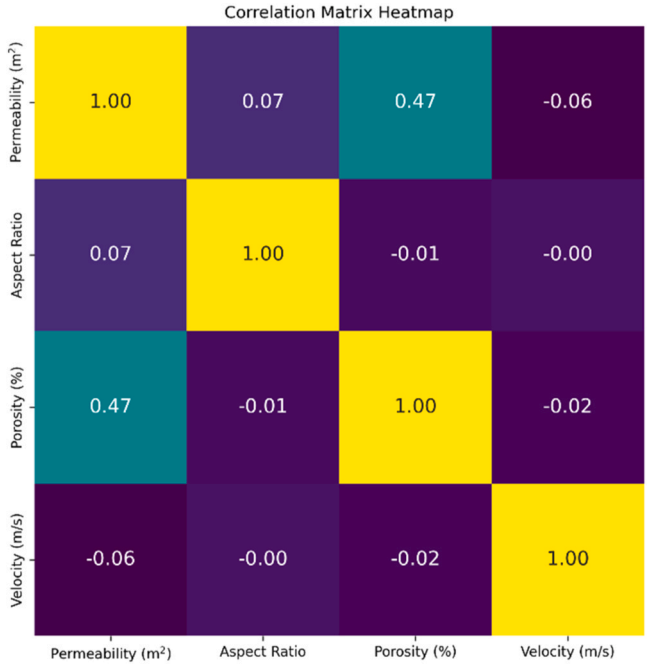


Fig. 9. Correlation Matrix Heatmap.

2.4. Feature extraction

The features of the permeability data included scaffold topology, porosity, aspect ratio and inlet velocity. These parameters represent the dominant geometric and flow-related factors governing fluid transport through porous scaffolds. To enhance ML model performance, additional feature-engineered variables were introduced based on physical insight. These included the square and cubic powers of porosity, which are commonly associated with nonlinear permeability–porosity relationships. In addition, the Kozeny-Carman inspired empirical feature was incorporated, providing an approximate permeability descriptor as a function of cubic porosity, square-root porosity, and aspect ratio. This physics-informed feature was included to embed prior knowledge of porous media flow behaviour into the learning process and to improve model generalisation.

2.5. Machine learning modelling

This problem is formulated as a supervised regression task, where permeability served as the target variable and the extracted geometric and flow features constituted the model inputs. All ML modelling was implemented in Python 3.12.3 using Scikit-learn library for conventional regression algorithms, PyTorch for neural network development, and Optuna for automated hyperparameter optimisation.

The complete 1005 dataset was randomly partitioned into training (80%) and testing (20%) subsets. The training set was used for model fitting, while the test set was reserved exclusively for evaluating predictive performance on previously unseen data. To ensure reproducibility, a random seed of 42 was applied throughout the data workflow.

Table 6
CFD model setup validation.

	Inlet Velocity	Porosity	Aspect Ratio	Permeability $\times 10^{-8}$ k_{CFD}	Permeability $\times 10^{-8}$ k_{lit}	Relative Error $\lvert k_{lit} - k_{CFD}\rvert / k_{lit}$
Cracknell et al. [53]	40 mm·s^{-1}	61.0%	1:1	2.573	2.34 (experiment)	9.97%
					2.44 (numerical)	5.36%
		57.1%	1:0.75	1.373	1.20 (experiment)	14.4%
					1.37 (numerical)	0.232%
		66.0%	1:1.5	5.25	4.84 (experiment)	8.43%
					4.67 (numerical)	12.4%
Gupta et al. [54]	0.7 mm·s^{-1}	76.5%	1:1	3.110	2.86	8.74%
		68.9%	1:1	2.309	2.19	5.43%
		61.4%	1:1	1.697	1.65	2.85%

Table 7
Model performance for tested algorithms.

Algorithm	In-Sample RMSE	In-Sample R^2	Out-of-Sample RMSE	Out-of-Sample R^2
Linear	3.888248×10^{-8}	0.795797	4.001905×10^{-8}	0.779201
Decision Tree	$\mathbf{7.360986 \times 10^{-23}}$	**1.000000**	$\mathbf{7.774255 \times 10^{-9}}$	**0.990900**
Random Forest	$\mathbf{2.101198 \times 10^{-9}}$	**0.999404**	$\mathbf{6.397342 \times 10^{-9}}$	**0.993939**
Gradient Boosting	$\mathbf{9.199994 \times 10^{-9}}$	**0.988568**	$\mathbf{1.085773 \times 10^{-8}}$	**0.983440**
Lasso	9.409728×10^{-8}	-0.195940	9.394632×10^{-8}	-0.198559
Ridge	3.863382×10^{-8}	0.798400	3.958658×10^{-8}	0.783964
SVR	1.147214×10^{-8}	0.982224	1.419474×10^{-8}	0.971157
KNeighbours	7.802703×10^{-8}	0.991777	1.576374×10^{-8}	0.963944

Table 8
Cross-validated RMSE for optimised tree-based models.

Algorithm	Optimised RMSE
Decision Tree	8.3465×10^{-9}
Random Forest	6.4887×10^{-9}
Gradient Boosting	3.3512×10^{-9}

Table 9
Optimised Hyperparameter configurations for Gradient Boosting.

Hyperparameter	Configuration
regressor__reg__subsample	0.8
regressor__reg__n_estimators	800
regressor__reg__min_samples_split	5
regressor__reg__min_samples_leaf	5
regressor__reg__max_features	None
regressor__reg__max_depth	5
regressor__reg__learning_rate	0.1

Table 10
Cross-validated performance of optimised Gradient Boosting.

Metric	Performance
RMSE	3.3512×10^{-9}
MAE	1.6492×10^{-9}
R^2	0.9985
RMSLE	4.1862×10^{-2}

While this work focused primarily on developing an ANN model, a comparison with classical ML models—including regression and tree-based algorithms—was also conducted to provide a necessary baseline for performance evaluation. The baseline models considered included eight ML models: Linear regression, Ridge regression, Lasso regression, Support Vector Regression, K-nearest neighbours, Decision tree, Random Forest and Gradient boosting.

Prior to model training, a series of data preprocessing operations were applied to improve numerical stability and facilitating patterns recognition by the ML algorithms. The permeability values were transformed into logarithmic space during training to linearise the exponential trend. Final permeability predictions were subsequently obtained by applying an inverse transformation for physical interpretability. To prevent data leakage, all preprocessing transformations were fitted exclusively on the training dataset and then applied unchanged to the test dataset. Each algorithm on default hyperparameter settings were trained on the same training set, and in-sample and out-of-sample performance via cross-validation with five folds were compared with root mean squared error (RMSE) and coefficient of determination (R^2) metrics. Fig. 5 shows the baseline comparison for classical ML algorithms fitted under default hyperparameters, where it appears that tree-based methods dominate in terms of in-sample and out-of-sample RMSE.

The tree-based algorithms that demonstrated strong baseline performance were shortlisted for subsequent hyperparameter optimisation later using a randomised search strategy. Model tuning was performed using five-fold cross-validation, with 200 random hyperparameter configurations evaluated for each shortlisted model, totalling at 1000 fits.

An ANN based on a multilayer perceptron (MLP) architecture was selected as the primary learning model in this study. The network consists of an input layer, one or more hidden layers, and an output layer. Trainable weightings and activation functions associated in the arcs that connect neurons between adjacent layers optimised using back-propagation, a form of gradient descent. This algorithm was chosen for its lightweight efficiency relative to other ANN algorithms and its abilities to generalise data with high accuracy on relatively lower data samples.

Consistent with the baseline algorithms, permeability values were log-transformed prior to ANN training. However, unlike the classical ML approaches, the categorical feature was vectorised using embedding layers (with three dimensions), and the numerical features were scaled uniformly to the [0,1] range on a per-feature basis before training.

Similar to the baseline algorithms, both in-sample and out-of-sample predictive performance were evaluated with RMSE and R^2 metrics, and hyperparameter tuning with Optuna was used to optimise the MLP model through Bayesian Optimisation over 40 trials. Model training employed a minibatch gradient descent strategy, with the Adam optimiser to iteratively minimise the loss function during backpropagation. An early stopping scheme was incorporated into the training loop to

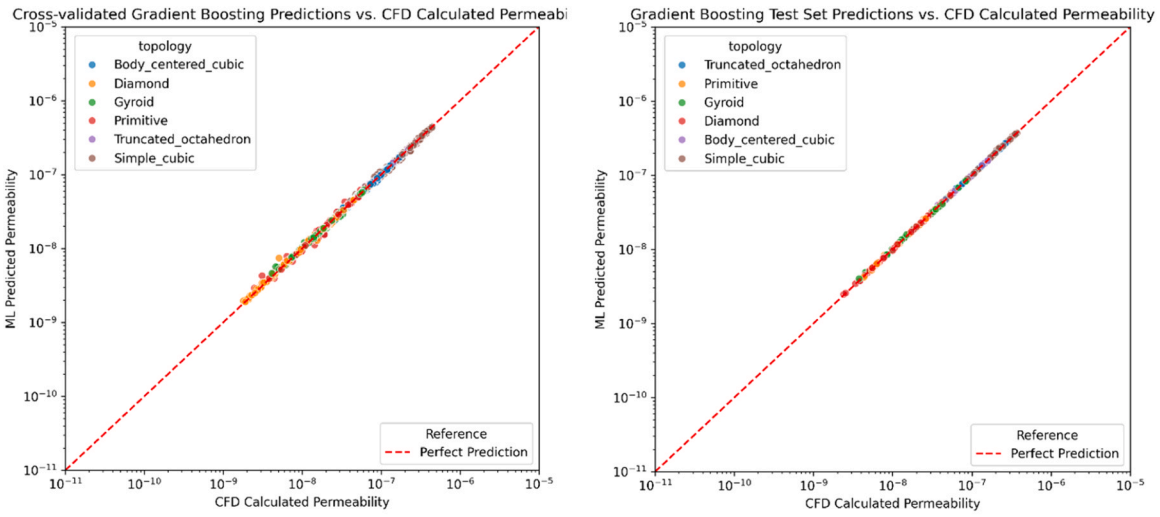


Fig. 10. Gradient Boosting Predicted vs CFD permeability for (a) Training set (b) Test set.

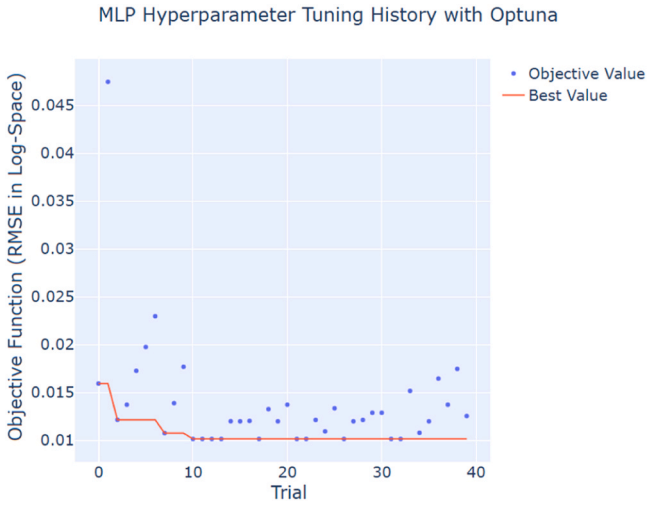


Fig. 11. MLP Optimisation History with Optuna.

Table 11
Optimised Hyperparameter configurations for MLP.

Hyperparameter	Configuration
num_epoch	1400
learning_rate	0.00015
batch_size	16
architecture	[128, 64, 32, 16]

Table 12
Averaged Cross-validated performance for optimised MLP.

Metric	Performance
RMSE	2.6994×10^{-9}
MAE	1.3168×10^{-9}
R^2	0.9989
RMSLE	1.0164×10^{-9}

prevent overfitting. This was implemented by computing the averaged cross-validated RMSE every 20 epochs during training, with early termination if no improvement was observed for five consecutive evaluations, referred as patience. The Rectified Linear Unit (ReLU) activation function was used in the hidden layers due to their computational efficiency and favourable convergence behaviour. Five-fold cross-validation was incorporated into the training loop to assess generalisation performance. The hyperparameters that were tuned included the number of epochs, minibatch size, learning rate and the MLP network topology. Tables 2–5 presents the search space for different machine learning algorithms.

Verification and validation of both the classical ML and ANN algorithms were conducted to ensure that the relationships and patterns learned reflect meaningful physical behaviour rather than statistical artefacts. This was achieved by prioritising minimisation of out-of-sample RMSE during cross-validation, supplemented by standard diagnostic analyses including residual and error distribution inspection, Q–Q plots for normality assessment, and permutation testing to confirm the absence of data leakage. The trained models were then used to predict the permeability of the test set with unseen geometry descriptors and flow velocities, along with an external set of data from literature.

3. Results and discussion

3.1. CFD results

Fig. 6 illustrates the pressure and velocity contours of the fluid volume through each of the different porous scaffold media, with 1:1 aspect ratio and 80% porosity. It is observed that the TPMS topologies (Primitive, Gyroid and Diamond) generally possess an increased pressure drop due to their naturally higher tortuosity in comparison to the lattice-based graph topologies. The volume rendering of graph topologies indicates that fluid flows vertically without resistance, resulting in a lower pressure drop. Fig. 7 supports this observation, as the pressure gradient for all TPMS topologies in this study appears to be higher, and the spread within each velocity group is attributed to varying aspect ratios.

3.2. Dataset characteristics

The permeability trend for all scaffold topologies and variants over porosity is illustrated in Fig. 8. Darcy's law was applied regardless of the Reynolds number, and the consequences are discussed later. There is a clear non-linear trend, showing permeability exponentially increasing

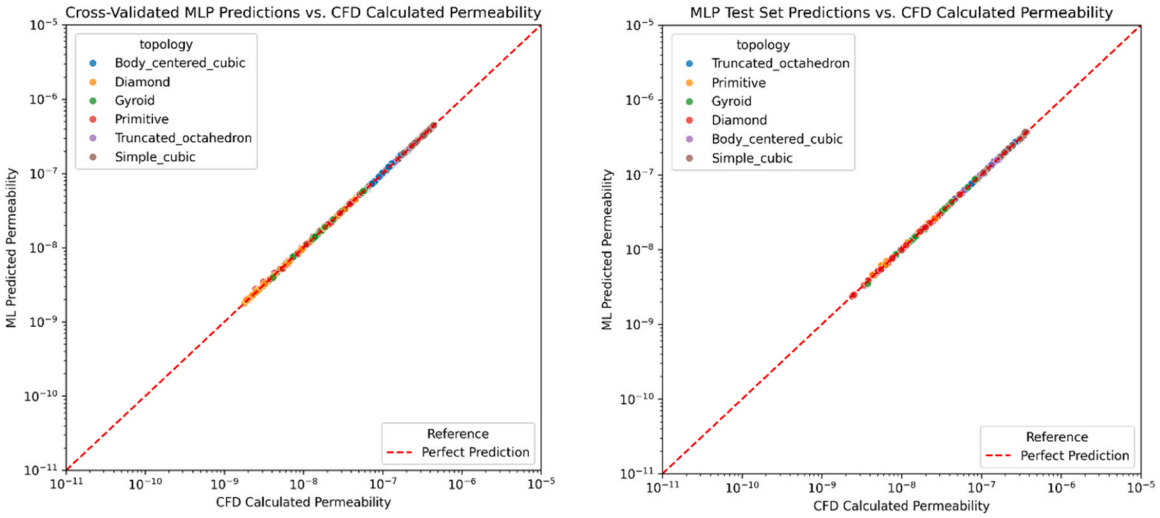


Fig. 12. MLP Predicted vs CFD permeability for (a) Training set (b) Test set.

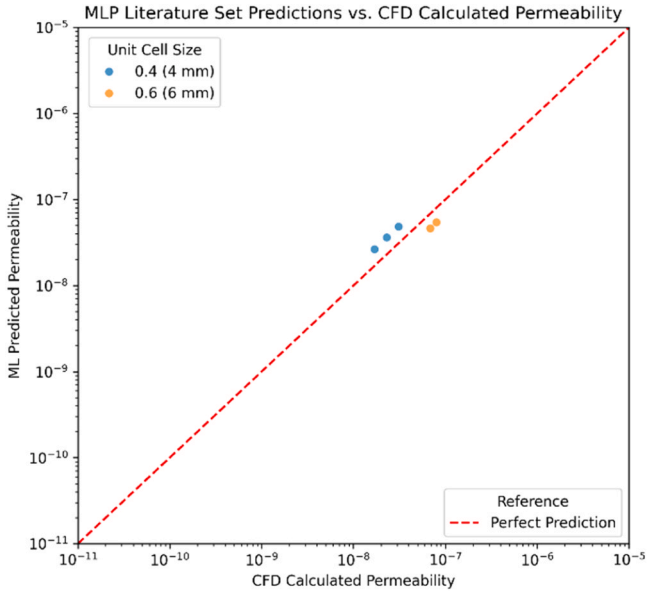


Fig. 13. MLP model validation with [54].

with porosity, albeit at different rates which are attributed by the scaffold topology and aspect ratio. The effects of aspect ratio were apparent, and the spread is highly dependent on the scaffold topology. For example, the Primitive structure exhibited relatively less variation with aspect ratio compared with the Diamond topology. This exponential behaviour motivated a logarithmic transform for permeability during data preprocessing to mitigate skewness and improve model robustness.

The area in red under each aspect ratio and scaffold topology is a result of varying flow velocities. The difference is fully attributed to the increased inertial forces present in higher flow speeds, and Darcy's law is no longer applicable to evaluating permeability, instead requiring an evaluation of Forchheimer coefficient to explain the variation. Visually, it appears that a velocity of 1.0 mm·s^{-1} and 0.1 mm·s^{-1} gives the same permeability values for most cases, with slight deviations for increasing porosity. The lower points indicate a decreased apparent permeability due to increased flow velocity, exceeding Re $>$ 1. For topologies with generally higher pore sizes, which are Simple Cubic and Primitive, a further separation was observed between 0.1 and 1.0 mm·s^{-1} flow speeds for higher porosities, indicating that a 1.0 mm·s^{-1} introduced inertial effects greater due to higher Reynolds number.

Fig. 9 presents a correlation analysis of the entire dataset, in which have indicated that porosity as the dominant predictor of Darcy permeability ($r \approx 0.47$), which is supported by Fig. 8, where an exponential trend was observed between permeability and porosity in all topologies. Aspect ratio has a weaker attribution to permeability ($r \approx 0.07$), as topologies such as primitive, body centered cubic and simple cubic are shown to have significant overlap with different aspect ratios. Velocity is shown to have a negative influence on permeability ($r \approx -0.06$), which aligns with Fig. 8, where the Darcy permeability decreased with increased velocity.

3.3. CFD validation

The benchmark cases replicated from external literature findings are shown in Table 6. The fluid material properties, and unit cell size configurations of the CFD pipeline developed in this study were adjusted to match the benchmark cases, thereby minimising discrepancies.

The model setup appears to generally agree with literature results, with most benchmark cases having a relative error of less than 10%. The model appears to overestimate permeability as porosity increases. The high deviations are partially attributed to the inconsistencies in the gyroid scaffold generation by Gupta et al. [54], who employed SolidWorks 2016 which creates gyroid structures that are fundamentally different from nTop. The gyroid structures generated by SolidWorks appear to have increased tortuosity, leading to lower permeability values. In addition, they employ a no-slip boundary condition to the walls of the rectangular volume, contrasting to symmetrical boundary condition used in this report. This potentially the partial attributed deviations due to boundary effects of different boundary conditions used.

3.4. ML model performance

Among all tested classical algorithms with default hyperparameters, the tree-based methods (Decision Tree, Random Forest and Gradient Boosting) stood out with the best balance of predictive accuracy and generalisation, where all three methods achieved an In-sample and Out-of-Sample RMSE of $< 1.1 \times 10^{-8}$ and an R^2 of > 0.98 as shown in Table 7.

The hyperparameter tuning results are summarised in Table 8,

showing that Gradient Boosting outperforms the other tree-based algorithms after optimisation with randomised search. The optimised hyperparameter configurations is listed in Table 9, and the cross-validated R^2, Mean Absolute Error (MAE) and Root Mean Squared Log Error (RMSLE) metrics are shown in Table 10. The results indicate that 99.8% of cross-validated variance in the training data was explained by the Gradient Boosting algorithm as shown in Fig. 10(a), where the ML and CFD evaluated permeabilities are closely matched along 1:1 parity line. There appears to be marginal deviations at lower permeabilities that correspond to the TPMS topologies. The exceptionally high R2 and low RMSE on the training set are primarily a consequence of the deterministic and highly structured nature of the CFD-generated dataset, which is free of experimental noise and spans smooth, low-dimensional parametric variations within each unit cell family. Although the dataset includes multiple topology classes with different tortuosities and pore throat distributions, these classes are sampled in a controlled manner, allowing the model to accurately learn topology-specific trends rather than being challenged by stochastic variability

The model prediction for the independent, unseen test set is illustrated in Fig. 10(b), where an RMSE of 2.13×10^{-9} and an R^2 of 0.9993 were measured, indicating a strong generalisation was achieved for similar but unseen geometry and flow scenarios. Interestingly, the training R^2 is slightly lower than the test R^2, likely due to random variation in the 80/20 split, where the test data may genuinely contain easier to predict cases.

The hyperparameters of the MLP model was optimised with Optuna, and Fig. 11 shows the progressive minimisation of the objective function with sequential hyperparameter selection. The minimised solution was found as early as in the 10th trial, and the detail of the optimised configuration is listed in Table 7. The complete hyperparameter-tuning process required slightly more than three hours, corresponding to an average of approximately 4.6 min per trial, or about 55 s per fold (across five folds), in addition to the intermittent validation evaluations performed for early-stopping checks.

The optimised hyperparameters of the MLP follows Table 11, and the cross-validated performance after optimisation are shown in Table 12, where an RMSE of 2.70×10^{-9} and an R^2 of 0.9989 was achieved on the training set, as shown in Fig. 11. There is a very marginal improvement in the averaged cross-validated R^2 with the MLP model over Gradient Boosting, which already has a near perfect predictive and generalisation performance. The MLP prediction for unseen test data is displayed in Fig. 12(b), where an RMSE of 1.93e-09 and an R^2 of 0.9994 was achieved, performing marginally worse than Gradient Boosting in terms of absolute error and prediction variance. Like Gradient Boosting, the test set achieved a marginally stronger R^2 and RMSE compared to the averaged cross-validated training set, likely attributed to discrepancies with the training and test target distributions.

The results indicate that the Gradient Boosting and MLP models learned the data exceptionally well, with both models averaging a cross-validation R^2 of greater than 0.998, as well as strong regularisation that enabled strong generalisation with unseen test data. While Gradient Boosting performed very marginally better than the MLP model with unseen test data, repeated runs over different seeds would be beneficial in analysing the sensitivity of the models arising from the random 80/20 split performed at the data preprocessing stage.

The model was tested on external data sourced from literature, namely permeability data [54] due similarities with the problem scenario in how the fluid material properties are similar. Although the unit cell sizes differ, equal porosities were assumed, and the discrepancies due to unit cell sizes were apparent as seen in Fig. 13. The 1:1 parity plot indicated that the ML predicted permeability was over-estimated for the 4 mm unit cell gyroids, and under-estimated for the 6 mm unit cell gyroids, resulting in an average error of 46.58%. However, this deviation matches the fact that the ML model in this studied was trained exclusively with 5 mm unit cells.

4. Conclusions

This study presents a fully automated hybrid CFD–machine learning framework for predicting the permeability of patient-specific 3D-printed bone scaffolds across a wide architectural design space. By integrating parametric CAD generation, high-fidelity CFD simulation, and supervised ML modelling within a unified Python-driven pipeline, the work addresses a central challenge in bone tissue engineering: the need for efficient, geometry-aware permeability estimation that scales to large candidate design sets. The framework successfully generated thousands of scaffold variants spanning six topologies, broad porosity and aspect ratio ranges, enabling a comprehensive synthetic dataset for surrogate model development.

The CFD simulations confirmed expected architectural influences on fluid transport—TPMS scaffolds exhibited higher tortuosity and pressure drops, while lattice-based structures demonstrated more streamlined flow behaviour. Permeability demonstrated a consistently nonlinear dependence on porosity across all geometries, validating the need for feature engineering and logarithmic transformations in the ML stage. Model validation against literature showed strong consistency, with most benchmark cases exhibiting $< 10\%$ relative error, supporting the reliability of the CFD configuration and workflow automation.

Among classical ML models, tree-based algorithms provided strong baseline performance, with Gradient Boosting achieving the most favourable balance between bias and variance after hyperparameter optimisation. The MLP-based ANN model achieved similarly high accuracy, with cross-validated R^2 values exceeding 0.9989 and test-set $R^2 > 0.9994$, demonstrating excellent generalisation to unseen cases. Although both models performed exceptionally on CFD-generated synthetic data, the external validation highlighted the sensitivity to unit cell size differences, underscoring the importance of training datasets that span broader morphological variations.

Overall, the proposed hybrid pipeline offers a robust and scalable approach to permeability prediction, reducing computational cost from hours per CFD simulation to near real-time surrogate model inference. This capability supports rapid pre-operative optimisation of anatomy-informed or application-specific scaffold designs and facilitates design exploration across complex, multi-parameter spaces that would be impractical using CFD alone.

CRediT authorship contribution statement

Maedeh Amirpour: Writing – review & editing, Writing – original draft, Visualization, Validation, Supervision, Resources, Project administration, Investigation, Funding acquisition, Formal analysis, Data curation, Conceptualization. **Eric Feng:** Writing – original draft, Validation, Methodology, Formal analysis, Data curation, Conceptualization. **Ali Entezari:** Writing – review & editing, Supervision, Software, Investigation, Conceptualization.

Declaration of Competing Interest

The authors declare that they have no known competing financial interests or personal relationships that could have appeared to influence the work reported in this paper.

Acknowledgment

This work is funded by the Research Development Fund from the University of Auckland, which covers all costs associated with this research. This research did not receive any specific grant from external funding agencies in the public, commercial, or not-for-profit sectors.

The authors would like to acknowledge the contributions of Hannah Huddleston and Cindy Leung, who performed data collection carried out for this work as part of their part IV project.

Data Availability

Data will be made available on request.

References

[1] S. Toosi, M.J. Javid-Naderi, A. Tamayol, M.H. Ebrahimzadeh, S. Yaghoubian, S. A. Mousavi Shaegh, Additively manufactured porous scaffolds by design for treatment of bone defects, Front. Bioeng. Biotechnol. 11 (2024) 1252636.

[2] F. Migliorini, G. La Padula, E. Torsiello, F. Spiezia, F. Oliva, N. Maffulli, Strategies for large bone defect reconstruction after trauma, infections or tumour excision: a comprehensive review of the literature, Eur. J. Med. Res. 26 (1) (2021) 118.

[3] O. Ntousi, M. Roumpi, P.K. Siogkas, D. Polyzos, I. Kakkos, G.K. Matsopoulos, D. I. Fotiadis, Advances in computational modeling of scaffolds for bone tissue engineering: A narrative review of the current approaches and challenges, Biomechanics 5 (4) (2025) 76.

[4] S. Wu, X. Liu, K.W. Yeung, C. Liu, X. Yang, Biomimetic porous scaffolds for bone tissue engineering, Materials Science Engineering R Reports 80 (2014) 1–36.

[5] G. Paltanea, V. Manescu, I. Antoniac, A. Antoniac, I.V. Nemoianu, A. Robu, H. Dura, A review of biomimetic and biodegradable magnetic scaffolds for bone tissue engineering and oncology, Int. J. Mol. Sci. 24 (5) (2023) 4312.

[6] H. Guo, Q. Li, H. Zreiqat, A. Entezari, Emerging technologies for personalised oro-maxillofacial bone regeneration: Design strategies and fabrication techniques, Biomaterials (2025) 123709.

[7] D. Ali, S. Sen, Computational fluid dynamics study of the effects of surface roughness on permeability and fluid flow-induced wall shear stress in scaffolds, Ann. Biomed. Eng. 46 (12) (2018) 2023–2035.

[8] M. Bedding-Tyrrell, N. Khatri, P. Nithiarasu, B. Sandnes, P. Egan, F. Zhao, Data-driven calculation of porous geometry-dependent permeability and fluid-induced wall shear stress within tissue engineering scaffolds, J. Eng. Des. 36 (10) (2025) 1631–1645.

[9] M. Ebrahimi, Porosity parameters in biomaterial science: Definition, impact, and challenges in tissue engineering, Front. Mater. Sci. 15 (3) (2021) 352–373.

[10] G. Chiou, E. Jui, A.C. Rhea, A. Gorthi, S. Miar, F.M. Acosta, T. Guda, Scaffold Architecture and Matrix Strain Modulate Mesenchymal Cell and Microvascular Growth and Development in a Time Dependent Manner: Chiou et al, Cell. Mol. Bioeng. 13 (5) (2020) 507–526.

[11] F. Caiazzo, V. Alfieri, B.D. Bujazha, Additive manufacturing of biomorphic scaffolds for bone tissue engineering, Int. J. Adv. Manuf. Technol. 113 (9) (2021) 2909–2923.

[12] A. Amirian, M. Battley, O. Diegel, M. Amirpour, Additive manufacturing defects in polymeric lattice structures: a comprehensive analysis of morphology, distribution, and printing orientation influence, Int. J. Adv. Manuf. Technol. 140 (9) (2025) 5361–5384.

[13] M. Amirpour, S. Bickerton, E. Calius, R. Das, B. Mace, Numerical and experimental study on deformation of 3D-printed polymeric functionally graded plates: 3D-digital image correlation approach, Compos. Struct. 211 (2019) 481–489.

[14] M. Amirpour, D. Cracknell, A. Amirian, A.N. Alipour, Hybrid 3D printing of fluid-filled lattices for biomedical applications: a review, Int. J. Adv. Manuf. Technol. 136 (10) (2025) 4083–4105.

[15] L. Zhang, B. Song, J. Zhang, Y. Yao, J. Lu, Y. Shi, Decoupling microlattice metamaterial properties through a structural design strategy inspired by the Hall–Petch relation, Acta Mater. 238 (2022) 118214.

[16] X. Yuan, G. Li, L. Zhang, J. Song, J. Chen, J. Zheng, Y. Shi, Spatial orientation on manufacturing fidelity and mechanical-transport-biological performances of 3D-printed microlattice structures, Compos. Struct. 372 (2025) 119551.

[17] A. Amirian, M. Battley, M. Amirpour, Characterisation of process-induced defects in polymeric strut-based lattice structures produced by the powder bed fusion additive manufacturing process, Rapid Prototyp. J. 31 (8) (2025) 1656–1674.

[18] D. Cracknell, M. Battley, J. Fernandez, M. Amirpour, The mechanical response of polymeric gyroid structures in an optimised orthotic insole, Biomech. Model. Mechanobiol. 24 (1) (2025) 311–329.

[19] D. Cracknell, M. Battley, J. Fernandez, M. Amirpour, Static and dynamic optimisation of fluid-filled responsive orthotic insoles, Biomech. Model. Mechanobiol. 24 (2) (2025) 713–741.

[20] A. Timercan, V. Sheremetyev, V. Brailovski, Mechanical properties and fluid permeability of gyroid and diamond lattice structures for intervertebral devices: functional requirements and comparative analysis, Sci. Technol. Adv. Mater. 22 (1) (2021) 285–300.

[21] A.P.G. Castro, T. Pires, J.E. Santos, B.P. Gouveia, P.R. Fernandes, Permeability versus design in TPMS scaffolds, Materials 12 (8) (2019) 1313.

[22] S. Nie, P. Liu, K. Chen, W. Wang, Y. Chen, B. Bate, Permeability of structured porous media: numerical simulations and microfluidic models, J. Zhejiang Univ. Sci. A 25 (12) (2024) 1018–1036.

[23] A.R. de Castro, M. Chabanon, B. Goyeau, Numerical analysis of the fluid-solid interactions during steady and oscillatory flows of non-Newtonian fluids through deformable porous media, Chem. Eng. Res. Des. 193 (2023) 38–53.

[24] A.A. Acar, E. Daskalakis, P. Bartolo, A. Weightman, G. Cooper, G. Blunn, B. Koc, Customized scaffolds for large bone defects using 3D-printed modular blocks from 2D-medical images, BioDes. Manuf. 7 (1) (2024) 74–87.

[25] A. Wagner, E. Eggenweiler, F. Weinhardt, Z. Trivedi, D. Krach, C. Lohrmann, I. Rybak, Permeability estimation of regular porous structures: a benchmark for comparison of methods, Transp. Porous Media 138 (1) (2021) 1–23.

[26] T. Ozgumus, M. Mobedi, U. Ozkol, Determination of Kozeny constant based on porosity and pore to throat size ratio in porous medium with rectangular rods, Eng. Appl. Comput. Fluid Mech. 8 (2) (2014) 308–318.

[27] B. Zhang, Computational fluid dynamics analysis of the fluid environment of 3D printed gradient structure in interfacial tissue engineering, Med. Eng. & Phys. 128 (2024) 104173.

[28] A. Entezari, N.C. Liu, I. Roohani, Z. Zhang, J. Chen, B. Sarrafpour, Q. Li, On design for additive manufacturing (DAM) parameter and its effects on biomechanical properties of 3D printed ceramic scaffolds, Mater. Today Commun. 23 (2020) 101065.

[29] Z. Zhao, F. Melke, J. Ito, K. Van Rietbergen, B, S. Hofmann, A multiscale computational fluid dynamics approach to simulate the micro-fluidic environment within a tissue engineering scaffold with highly irregular pore geometry, Biomech. Model. Mechanobiol. 18 (6) (2019) 1965–1977.

[30] E. Drioli, L. Giorno (Eds.), Encyclopedia of membranes, Springer Berlin Heidelberg, Berlin, 2016, pp. 818–819.

[31] Sobieski, W., & Zhang, Q. (2014). Sensitivity analysis of Kozeny-Carman and Ergun equations. Technical Sciences/University of Warmia and Mazury in Olsztyn.

[32] M. Rehman, M.B. Hafeez, M. Krawczuk, A comprehensive review: Applications of the Kozeny–Carman model in engineering with permeability dynamics, Arch. Comput. Methods Eng. 31 (7) (2024) 3843–3855.

[33] K. Vhora, D. Thévenin, G. Janiga, K. Sundmacher, CFD analysis of the flow in Schwarz-D TPMS structures for engineering applications, Chem. Ing. Tech. 96 (12) (2024) 1683–1696.

[34] Z.Y. Zhang, H. Zhang, J. Zhang, S.K. Qin, M.D. Duan, Study on flow field characteristics of TPMS porous materials, J. Braz. Soc. Mech. Sci. Eng. 45 (4) (2023) 188.

[35] S. Gabetti, B. Masante, A. Schiavi, E. Scatena, E. Zenobi, S. Israel, D. Massai, Adaptable test bench for ASTM-compliant permeability measurement of porous scaffolds for tissue engineering, Sci. Rep. 14 (1) (2024) 1722.

[36] J. Tian, C. Qi, Y. Sun, Z.M. Yaseen, B.T. Pham, Permeability prediction of porous media using a combination of computational fluid dynamics and hybrid machine learning methods, Eng. Comput. 37 (4) (2021) 3455–3471.

[37] H.S. N. Musthafa, J. Walker, Design of Trabecular Bone Mimicking Voronoi Lattice-Based Scaffolds and CFD Modelling of Non-Newtonian Power Law Blood Flow Behaviour, Computation 12 (12) (2024) 241.

[38] W. Jiao, D. Scheidweiler, N. Delouche, P. de Anna, A. Guadagnini, Intrinsic permeability of heterogeneous porous media, Phys. Rev. Fluids 9 (9) (2024) 094102.

[39] M. Bedding-Tyrrell, N. Khatri, P. Nithiarasu, B. Sandnes, P. Egan, F. Zhao, Data-driven calculation of porous geometry-dependent permeability and fluid-induced wall shear stress within tissue engineering scaffolds, J. Eng. Des. 36 (10) (2025) 1631–1645.

[40] M. Rehman, M.B. Hafeez, M. Krawczuk, A comprehensive review: Applications of the kozeny–carman model in engineering with permeability dynamics, Arch. Comput. Methods Eng. 31 (7) (2024) 3843–3855.

[41] H. Shen, C. Song, L. Yang, Dual-objective customized design of mechanical responses and mass transport characteristics for TPMS bone scaffolds, Int. J. Mech. Mater. Des. 22 (1) (2026) 5.

[42] B. Coburn, R.R. Salary, Computational fluid dynamics modeling of material transport through triply periodic minimal surface scaffolds for bone tissue engineering, J. Biomech. Eng. 147 (3) (2025) 031007.

[43] H. Wang, Y. Lyu, J. Jiang, H. Zhu, Data-driven inverse design of novel spinodoid bone scaffolds with highly matched mechanical properties in three orthogonal directions, Mater. & Des. 251 (2025) 113697.

[44] S. Ibrahimi, L. D'Andrea, D. Gastaldi, M.W. Rivolta, P. Vena, Machine Learning approaches for the design of biomechanically compatible bone tissue engineering scaffolds, Comput. Methods Appl. Mech. Eng. 423 (2024) 116842.

[45] R. Gabrieli, A. Schiavi, F. Baino, Determining the permeability of porous bioceramic scaffolds: significance, overview of current methods and challenges ahead, Materials 17 (22) (2024) 5522.

[46] R. Asbai-Ghoudan, S.R. de Galarreta, N. Rodriguez-Florez, Analytical model for the prediction of permeability of triply periodic minimal surfaces, J. Mech. Behav. Biomed. Mater. 124 (2021) 104804.

[47] H. Montazerian, M. Zhianmanesh, E. Davoodi, A.S. Milani, M. Hoorfar, Longitudinal and radial permeability analysis of additively manufactured porous scaffolds: Effect of pore shape and porosity, Mater. & Des. 122 (2017) 146–156.

[48] I. Akbar, A.T. Prakoso, Y. Martino Astrada, M.S. Sinaga, M.I. Ammarullah, D. Adanta, H. Basri, Permeability study of functionally graded scaffold based on morphology of cancellous bone, Malays. J. Med. & Health Sci. 17 (2021).

[49] S. Salles, J. Shepherd, H.J. Vos, G. Renaud, Revealing intraosseous blood flow in the human tibia with ultrasound, JBMR 5 (2021) e10543.

[50] H. Liu, L.L. Liu, J.H. Tan, Y.G. Yan, J.B. Xue, Definition of Pore Size in 3D-Printed Porous Implants: A Review, ChemBioEng Rev. 10 (2) (2023) 167–173.

[51] K. Vhora, D. Thévenin, G. Janiga, K. Sundmacher, Numerical Investigation of Low-Reynolds-Number Flow in Double Schwarz-D TPMS Structure (August), in: Proceedings, 121, MDPI, 2025, p. 14 (August).

[52] S.S. Rathore, B. Mehta, P. Kumar, M. Asfer, Flow characterization in triply periodic minimal surface (TPMS)-based porous geometries: Part 1—Hydrodynamics, Transp. Porous Media 146 (3) (2023) 669–701.

[53] Cracknell, D. (2024). *Static and dynamic optimisation of fluid-filled lattices for responsive orthotic insoles* (Doctoral dissertation, ResearchSpace@ Auckland).

[54] A. Gupta, M. Rana, N. Mondal, Determining the optimal design parameters for gyroids using computational fluid dynamics analysis under a non-Newtonian perfusion system, Biomed. Eng. Adv. 9 (2025) 100153.